

Correlated insulators, density wave states, and their nonlinear optical response in magic-angle twisted bilayer graphene

Shihao Zhang,¹ Xin Lu,^{1,2} and Jianpeng Liu^{1,3,*}

¹*School of Physical Science and Technology, ShanghaiTech University, Shanghai 200031, China*

²*Laboratoire de Physique des Solides, Univ. Paris-Sud,*

Université Paris Saclay, CNRS, UMR 8502, F-91405 Orsay Cedex, France

³*ShanghaiTech laboratory for topological physics, ShanghaiTech University, Shanghai 200031, China*

The correlated insulator (CI) states and the recently discovered density wave (DW) states in magic-angle twisted bilayer graphene (TBG) have stimulated intense research interest. However, up to date, the nature of these “featureless” correlated states observed at different integer and fractional fillings of the flat bands are still elusive, which are lack of direct experimental characters. Thus an experimental probe to identify the characters of these featureless CI and DW states are urgently needed. In this work, we theoretically study the correlated insulators and density wave states at different integer and fractional fillings of the flat bands in magic-angle TBG based on extended unrestricted Hartree-Fock calculations including the Coulomb screening effects from the remote bands. We further investigate the nonlinear optical responses, such as second-harmonic generations and shift-current responses, of the various correlated states, and find that the different components of the nonlinear optical conductivities can be used to identify the nature of these CI and DW states at most of the fillings. Thus we propose nonlinear optical response as a unique experimental probe to unveil the nature of the peculiar CI and DW states discovered in experiments in magic-angle TBG.

Twisted bilayer graphene (TBG) system around the magic angle provides a promising platform to achieve various intriguing quantum phases such as the correlated insulators [1–10], orbital magnetic states and Chern-insulator states [7, 11–17], as well as unconventional superconductivity [2, 8–10, 18–21]. Near the magic angle 1.05° [22], there are two low-energy flat bands per spin per valley which are associated with nontrivial topological properties [23–27]. As a result, the electron-electron Coulomb interactions prevail kinetic energy, and the interplay between the strong Coulomb correlations and the nontrivial topology inherited from the Landau-level-like wavefunctions of the flat bands give rise to diverse correlated and topological states in this system, which have drawn significant attention from the theoretical community [28–46].

Most of the previous works have been focused on the integer fillings in the TBG system, and only a few pioneering works have paid attention to the fractional fillings of the flat bands [16, 47–50], which may realize unconventional density wave (DW) states [16, 47, 48] and even fractional Chern-insulator states [48]. However, up to date the nature of most of the “featureless” correlated insulator (CI) states observed at integer fillings such as the zero-Chern-number CIs at $\nu = 3, 0, \pm 2$ [1, 2], and the recently observed DW states at the fractional fillings $\nu = 7/2$, and $8/3$ [48]), are still elusive. An experimental probe to distinguish the characters of these featureless CI and DW states is needed.

In this work, we use extended unrestricted Hartree-Fock (HF) method within the subspace of the flat bands to study CIs and DW states at various fillings, including all integer fillings $-3 \leq \nu \leq 3$, and a few fractional

fillings $\nu = 8/3$ and $7/2$, at which unconventional CI and DW states are observed. The Coulomb potentials acted on the flat-band subspace from the remote bands have been taken into account [40], and the screening of Coulomb interactions in the flat-band space have been treated within constrained random phase approximation (cRPA). We have further studied different components of the nonlinear optical conductivities of these CI and DW states, and propose that the various competing correlated states in TBG can be unambiguously identified through the nonlinear optical responses such as second harmonic generation and shift-current measurements.

We first introduce the non-interacting Hamiltonian of TBG and the moiré superlattice geometries used in this work. In Fig. 1(a), the primitive moiré cell is marked the black rhombus; and the real-space moiré lattice vectors of the primitive cell, the doubled supercell, and the $\sqrt{3} \times \sqrt{3}$ tripled supercell are marked by black, red, and blue vectors respectively in Fig. 1(a); the corresponding reciprocal lattice vectors and moiré Brillouin zones of the three types of moiré supercells are marked in Fig. 1(b). All the calculations presented in this work are based on the superlattice structures presented in Fig. 1(a)-(b).

The low-energy effective Hamiltonian of the twisted bilayer graphene of valley μ ($\mu = \mp$ for K and K' valleys) is described by Bistritzer-MacDonald continuum model [22]:

$$H_\mu^0 = \begin{pmatrix} -\hbar v_F (\hat{\mathbf{k}} - \mathbf{K}_1^\mu) \cdot \sigma_\mu & U_\mu(\mathbf{r}) \\ U_\mu^\dagger(\mathbf{r}) & -\hbar v_F (\mathbf{k} - \mathbf{K}_2^\mu) \cdot \sigma_\mu \end{pmatrix}, \quad (1)$$

where v_F denotes the Fermi velocity, and the Hamiltonian is expanded near the Dirac points of the two layers \mathbf{K}_1^μ or \mathbf{K}_2^μ , with $\sigma_\mu = (\mu\sigma_x, \sigma_y, \sigma_z)$ ($\mu = \pm$) denoting Pauli matrices in the sublattice space. $U_\mu(\mathbf{r})$ refers to

the interlayer coupling matrix which introduces a slowly varying moiré potential to the system [51]. In Fig. 1(d) we show the energy bands of the continuum model of the K valley in the moiré Brillouin zone (mBZ) of the primitive cell, which can be classified into the flat bands near the charge neutrality point (CNP) and remote bands above and below them. These bands would be folded into the mBZs of the doubled and tripled supercells following the geometry shown in Fig. 1(b) [51]. Unless specified, we fix the twist angle $\theta = 1.05^\circ$ throughout this paper.

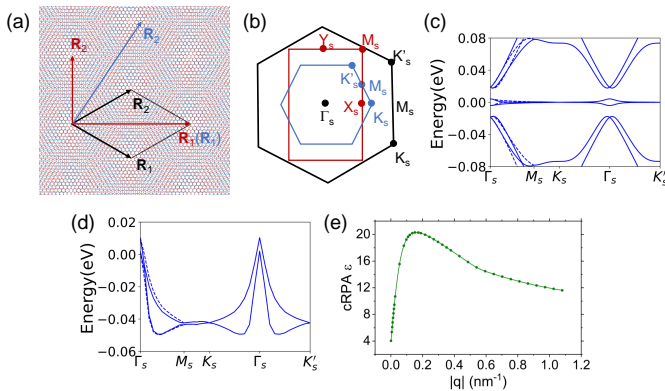


FIG. 1: (a) Illustration of the moiré superlattice of twisted bilayer graphene. The different layers are marked with red and blue colors. The lattice vectors of the primitive moiré cell, the doubled moiré supercell, and $\sqrt{3} \times \sqrt{3}$ moiré supercell are marked by black, red, and blue arrows respectively. (b) Moiré Brillouin zones of the primitive cell, doubled supercell, and $\sqrt{3} \times \sqrt{3}$ tripled supercell with high-symmetry points marked. (c) The non-interacting energy bands of the continuum model, and (d) the flat-band dispersions including effects of remote band Hartree-Fock potentials, where the solid and dashed lines denote bands from the K and K' valleys. (e) The wavevector dependence of the effective dielectric constant calculated by cRPA method.

Coulomb interaction and the screening effects.

— Now we consider the dominant long-range Coulomb interactions in the TBG system [51], which is expressed as

$$H_C = \frac{1}{2N_s} \sum_{\alpha\alpha'} \sum_{\mathbf{k}\mathbf{k}'} \sum_{\mathbf{q}\sigma\sigma'} V(\mathbf{q}) \hat{c}_{\mathbf{k}+\mathbf{q},\alpha\sigma}^\dagger \hat{c}_{\mathbf{k}'-\mathbf{q},\alpha'\sigma'}^\dagger \hat{c}_{\mathbf{k}',\alpha'\sigma'} \hat{c}_{\mathbf{k},\alpha\sigma} \quad (2)$$

where N_s denotes the total number of moiré cells in the entire system, \mathbf{k} and \mathbf{q} represent atomic wavevectors, α refers to the layer and sublattice indices, and σ refers to the spin index. A double-gate screened Coulomb interaction $V(\mathbf{q}) = e^2 \tanh(|\mathbf{q}|d_s) / (2\Omega_M \epsilon_{\text{BN}} |\mathbf{q}|)$ is adopted throughout this work, and here Ω_M is the area of moiré supercell, $d_s = 40$ nm is the thickness of the BN substrate and $\epsilon_{\text{BN}} \approx 4$ refers to background dielectric constant of the BN substrates. At small twist angles, the inter-site Coulomb interaction can be further divided into the intravalley section and the intervalley section, with the for-

mer being two orders of magnitudes larger than the latter. Thus we only consider the intravalley part of the Coulomb interactions, and further project them onto the flat bands of each valley. Then we self-consistently solve the interacting Hamiltonian $H_0 + H_C$ with unrestricted Hartree-Fock approximation, which will be extended to be adapted for a doubled moiré supercell for the cases of $\nu = 7/2, 1$ and 3 , and extended to the $\sqrt{3} \times \sqrt{3}$ tripled moiré supercell for $\nu = 8/3$. We study the ground state at $\nu = 3$ and 1 with a doubled moiré supercell in order to explain the observed CI state with zero Chern number [2, 48].

In Ref. 40 and Ref. 52, the authors propose to “regularize” the Coulomb interaction by subtracting a constant density $(1/2)\delta_{\mathbf{q},\mathbf{0}}$ from the density operator $\hat{\rho}(\mathbf{q})$, which reads

$$H'_C = \frac{N_s}{2} \sum_{\mathbf{q}} V(\mathbf{q}) \delta\hat{\rho}(\mathbf{q}) \delta\hat{\rho}(-\mathbf{q}), \quad (3)$$

in which $\delta\hat{\rho}(\mathbf{q})$ is defined as the density matrix at wavevector \mathbf{q} subtracted by a constant $(1/2)\delta_{\mathbf{q},\mathbf{0}}$ [51]. Note that Eq. (18) is not normal ordered, which differs from the normal ordered Hamiltonian only by a constant chemical-potential shift if all bands are included. However, if H'_C is projected onto a subset of low-energy bands, e.g., the flat bands, then Eq. (18) would be different from its normal ordered form H_C . By virtue of the particle-hole symmetry and $C_{2z}\mathcal{T}$ symmetry of the projected interaction Hamiltonian, the difference $\Delta H_C = H'_C - H_C$ can be re-expressed as the HF potentials from the remote bands exerted on the flat bands [40]. The remote band HF potentials ΔH_C would significantly change the dispersions of the flat bands. In Fig. 1(d), we present the flat band structures including remote-band HF potentials, from which it is evidently shown that the ΔH_C significantly enhances the overall bandwidth of flat bands and induces the particle-hole asymmetry.

In the double-gate screened Coulomb interaction $V(\mathbf{q})$, only the screening effect from the top and bottom gates has been taken into account, and we assume the gates are separated from the TBG device by BN layers with thickness $d_s = 40$ nm and dielectric constant $\epsilon_{\text{BN}} \approx 4$. The Coulomb interactions between electrons in the flat bands of TBG can be further screened by virtual excitations of particle-hole pairs from the remote bands, which contribute to a wave vector dependent dielectric constant, which we treat using the constrained random phase approximation:

$$\epsilon(\tilde{\mathbf{q}} + \mathbf{Q}) = \epsilon_{\text{BN}} (\mathbb{1} + \hat{\chi}^0(\tilde{\mathbf{q}}) \hat{V}(\tilde{\mathbf{q}}))_{\mathbf{Q},\mathbf{Q}}, \quad (4)$$

where $\hat{\chi}^0(\tilde{\mathbf{q}})$ is the zero-frequency bare susceptibility at moiré wavevector $\tilde{\mathbf{q}}$, and $\hat{V}(\tilde{\mathbf{q}})$ denotes the double-gate screened Coulomb interaction expressed in a matrix form, the details of which are presented in Supplementary Information [51]. The calculated effective dielectric constant as a function of wave vector $\mathbf{q} = \tilde{\mathbf{q}} + \mathbf{Q}$ (along the

$\Gamma_s - M_s$ direction, with flat-band filling factor $\nu=0$) is shown in Fig. 1(e). We see that the additional screening effects from the remote bands vanish as $\mathbf{q} \rightarrow \mathbf{0}$, i.e., $\lim_{\mathbf{q} \rightarrow \mathbf{0}} \epsilon(\mathbf{q}) \rightarrow \epsilon_{\text{BN}}$, and there is a peak of $\epsilon_{\text{BN}} \times \epsilon(\mathbf{q}) \sim 20$ for $\mathbf{q} \approx 0.2 \text{ nm}^{-1}$, consistent with previous report [53].

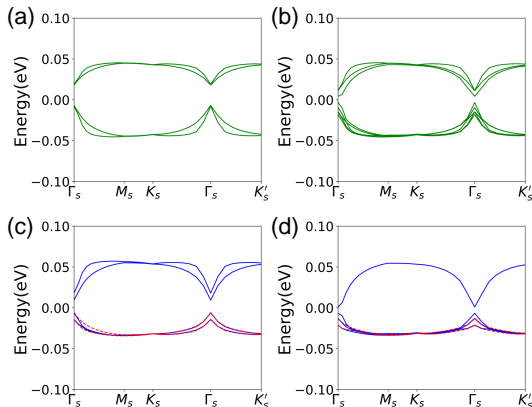


FIG. 2: The Hartree-Fock band dispersions at (a) $\nu=0$, (b) $\nu=1$ (c) $\nu=2$, and (d) $\nu=3$. At the filling $\nu=2$ and $\nu=3$, the energy bands from two valley are remarked with blue solid lines and red dash lines.

Correlated insulators at integer fillings. — We perform unrestricted HF calculations within the low-energy subspace of the flat bands including remote-band HF potentials, with the cRPA screened Coulomb interactions. We first study the ground states at integer fillings $-3 \leq \nu \leq 3$ without breaking moiré translational symmetry. With a realistic parameter choice of the intrasublattice interlayer coupling $u_0 = 0.079 \text{ eV}$ [54], our calculations reveal that the ground state at CNP is a Kramers intervalley coherent (K-IVC) state characterized by order parameters $(\tau_x, \tau_y)\sigma_y$ [32], with mixture of small valley polarization component $\langle \tau_z \rangle \approx 0.1$, where τ and σ denote Pauli matrices defined in the valley and sublattice space respectively, and $\langle \hat{O} \rangle$ denotes the expectation value of operator \hat{O} . Note that at integer filling $\nu = 0, 1, 2, 3$, the maximal valley polarization $|\langle \tau_z \rangle| = 4 - \nu$. In the chiral limit ($u_0 = 0$) with finite kinetic energy, a pure K-IVC state can be obtained at the CNP [51].

At $\nu = \pm 1$, with the realistic parameter choice, the HF ground state is also a mixed state with both K-IVC and valley polarized (SVP) orders with Chern number ± 1 , consistent with previous theoretical and experimental reports [12, 33, 41].

At $\nu = \pm 2$, with realistic parameter choice, we find that the ground state is a fully spin and valley polarized (SVP) state based on Hartree-Fock+cRPA calculations. However, if we take a fixed dielectric constant $\epsilon = 10$ without further including the screening effects from the remote bands, then the ground state at $\nu = 2$ involves three nearly degenerate states including an intervalley coherent state [51]. This indicates that the actual ground state at $\nu = 2$ is subtle, and can be sensitive to

TABLE I: Symmetries, order parameters and Chern numbers C for the ground states at integer fillings

fillings	main order parameters	symmetry	$\langle \tau_z \rangle$	C
$\nu=3$	$\tau_z, s_z, \tau_z s_z$	C_{3z}, C_{2x}	-1	1
$\nu=2$	$\tau_z, s_z, \tau_z s_z$	$C_{3z}, C_{2z}\mathcal{T}, C_{2x}$	-2	0
$\nu=1$	$(\tau_x, \tau_y)\sigma_y, \tau_z, s_z, \tau_z s_z$	C_{3z}	-0.85	1
$\nu=0$	$(\tau_x, \tau_y)\sigma_y, \tau_z$	C_{3z}	0.10	0
$\nu=-1$	$(\tau_x, \tau_y)\sigma_y, \tau_z, s_z, \tau_z s_z$	C_{3z}	1.14	-1
$\nu=-2$	$\tau_z, s_z, \tau_z s_z$	$C_{3z}, C_{2z}\mathcal{T}, C_{2x}$	-2	0
$\nu=-3$	$\tau_z, s_z, \tau_z s_z$	C_{3z}, C_{2x}	-1	-1

details of the system. Later we will show the nonlinear optical response can be used as a tool to identify the different types of CIs.

At $\nu = \pm 3$, the calculated HF ground state is always a SVP state with Chern number ± 1 . In Table I we present the dominant order parameters, symmetries, valley polarizations, and Chern numbers of the HF ground states preserving moiré translational symmetry at all integer fillings. We find that all of these CI states exhibit non-zero valley polarizations, which will contribute to nonlinear optical responses as will be discussed in detail below.

In Fig. 2(a)-(d) we present the Hartree-Fock band structures at $\nu = 0, 1, 2$, and 3. We find that the energy spectrum at CNP and $\nu = 1$ roughly preserves particle-hole symmetry, but for $\nu = 2, 3$ the conduction bands are more dispersive than the valence bands. The energy spectra at $\nu = -2, -3$ are exactly the opposite, with the valence bands being more dispersive than the conduction bands [51]. In a recent theoretical study [52], Kang *et al.* argued that such asymmetric single-particle dispersions in TBG are the origin of the cascade transitions observed in experiments [55, 56].

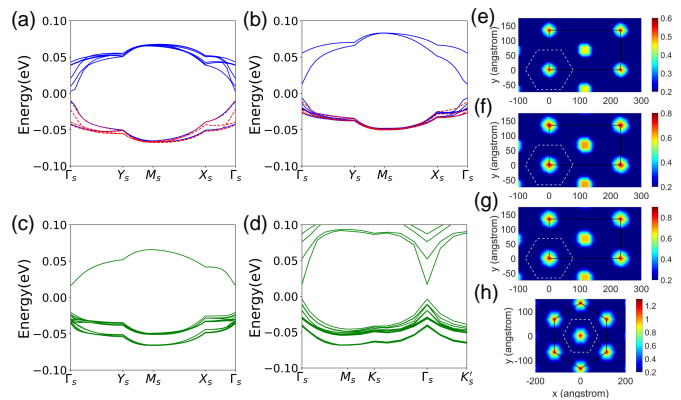


FIG. 3: (a) The energy bands of charge density wave state at the fillings $\nu = 1$ (a), $\nu = 3$ (b), $\nu = 7/2$ (c) and $\nu = 8/3$ (d). We also present the real-space distribution of charge density at the fillings $\nu = 1$ (e), $\nu = 3$ (f), $\nu = 7/2$ (g) and $\nu = 8/3$ (h). The Brillouin zone of primitive moiré lattice are drawn with white dash lines.

Density wave states — CI state with zero Chern number has been observed at $\nu = 3$ in TBG [2], which is inconsistent with previous theoretical results assuming preserved moiré translational symmetry [34, 35, 41]. Thus one naturally expects that the zero Chern number state at $\nu = 3$ may involve a spontaneous moiré translational symmetry breaking. Therefore, in this work we also perform HF calculations at $\nu = 3$ based on a doubled moiré supercell (see Fig. 1(a)-(b)). Moreover, motivated by the recent discoveries of correlated states at fractional fillings of the flat bands [48], we also study the possible DW states at $\nu = 1, 7/2$ and $8/3$.

Let us first consider the correlated DW state at $\nu = 3$ in TBG with doubled moiré supercell. The system still stays in the SVP phase at this filling, but there is one pair of unoccupied energy bands left due to the cell doubling. Since the pair of unoccupied energy bands belongs to same valley and same spin as shown in Fig. 3(b), the total Chern number of this SVP DW phase at $\nu = 3$ is zero, which is consistent with experimental results. The real-space charge density distribution of this DW state is inhomogeneous around the neighbouring *AA* sites, clearly breaks the primitive moiré translational symmetry, as shown in Fig. 3(f). We also study the possible DW state with doubled moiré supercell at $\nu = 1$, and the ground state is also a SVP state zero Chern number, with inhomogeneous charge distributions as shown in Fig. 3(e). Such a SPV DW state may explain the origin of the recently observed $C = 0$ state at $\nu = 1$ [48]. The HF band structures of these DW states with doubled primitive cell are presented in Fig. 3(a) ($\nu = 1$) and (b) ($\nu = 3$), where the solid blue lines and red dashed lines denote bands from the *K* and *K'* valleys respectively.

We continue to study the DW states at fractional fillings $7/2$ and $8/3$, which are calculated based on doubled ($\nu = 7/2$) and $\sqrt{3} \times \sqrt{3}$ tripled ($\nu = 8/3$) moiré supercells respectively. The calculated ground states at both $7/2$ and $8/3$ fillings are gapped, which may explain the experimentally observed CI with zero Chern number at $7/2$ filling, and the unusual $C = 1$ Chern insulator state at $\nu = 8/3$, as reported in Ref. 48. In particular, at $7/2$ filling, we find two nearly degenerate ground states: one is a spin-polarized K-IVC state with slight valley polarization and zero Chern number, and the other is a SVP state having Chern number 1. The energy difference between these two states $\sim 10 \mu\text{eV}$. We propose that the experimentally observed CI with zero Chern number at $7/2$ may be the spin polarized K-IVC state. The HF band structure of the spin polarized K-IVC DW state at $7/2$ filling is presented in Fig. 3(c). Such a state can be interpreted as follows. With doubled primitive moiré cells, there are two sets of the fourfold valley-spin degenerate flat bands, and the K-IVC order mixes the valleys within each set, opening a gap between the valence and conduction flat bands and trivializing the nontrivial band topology. Thus the K-IVC order parameter gives rise to

TABLE II: Symmetries, order parameters, valley polarizations $\langle \tau_z \rangle$, and K-IVC order amplitudes for the different DW states

fillings	main order parameters	symmetry	$\langle \tau_z \rangle$	IVC
$\nu = 1$	$\tau_z, s_z, \tau_z s_z$	$C_{2z} \mathcal{T}$	-6	0
$\nu = 3$	$\tau_z, s_z, \tau_z s_z$	$C_{2z} \mathcal{T}$	-2	0
$\nu = 7/2$	$(\tau_x, \tau_y) \sigma_y s_{0,z}, s_z$	\mathcal{T}'	0.07	0.45
$\nu = 8/3$	$(\tau_x, \tau_y) \sigma_y s_{0,z}, \tau_z, s_z, \tau_z s_z$	C_{3z}	3.65	0.54

8 conduction flat bands and 8 valence flat bands, all with zero Chern numbers for the doubled-cell system. At $7/2$ filling, 7 out of the 8 conduction flat bands are filled, yielding a spin polarized K-IVC state with zero Chern number.

At $8/3$ filling, based on $\sqrt{3} \times \sqrt{3}$ tripled supercell HF calculations, we find the ground state is a SVP state with moderate mixtures of K-IVC orders, and the calculated Chern number of this state is 1, which is also consistent with experimental report [48]. The Hartree-Fock band structures at $7/2$ and $8/3$ fillings are presented in Fig. 3(c) and (d) respectively. The corresponding ground-state real-space charge density distributions are presented in Fig. 3(g) ($\nu = 7/2$) and (h) ($\nu = 8/3$) respectively. The leading order parameters, symmetries, the calculated valley polarizations $\langle \tau_z \rangle$, and the calculated IVC order amplitudes in the different DW states at $\nu = 1, 3, 7/2$, and $8/3$ are presented in Table. II.

Nonlinear optical responses of the correlated states. — Quite a few of the experimentally observed CIs and DWs in magic-angle TBG are featureless insulating states, such as the CIs observed at CNP, $\nu = \pm 2$, the CI at $\nu = 3$, and the DW states at $7/2$. All of these states are just insulating with zero Chern number, and do not exhibit any further transport and optical characters. Therefore, it is difficult to experimentally identify the nature of these correlated states. Here we propose that these featureless correlated states may exhibit distinct nonlinear optical responses, which is described by the generation an AC current density $j^c(\omega_1 + \omega_2)$ due to the second-order response to the electric fields:

$$j^c(\omega_1 + \omega_2) = \sum_{a,b=x,y} \sigma_{ab}^c(\omega_1, \omega_2) E_a(\omega_1) E_b(\omega_2). \quad (5)$$

The nonlinear optical conductivity tensor σ_{ab}^c may serve as a unique probe to unveil the nature of the various correlated states observed in magic-angle TBG. In this work, we study two kinds of nonlinear optical processes, the shift-current response with $\omega_1 = -\omega_2 = \omega$, and the second harmonic generation (SHG) with $\omega_1 = \omega_2 = \omega$. For SHG response, the nonlinear susceptibility $\chi_{ab}^c(\omega) = i\sigma_{ab}^c(\omega)/(\epsilon_0 2\omega)$, where ϵ_0 is the vacuum permittivity.

We illustrate our idea by comparing the nonlinear optical responses of two prototypical CIs both with zero Chern numbers: a K-IVC state characterized by order

TABLE III: Four ordered states with non-vanishing nonlinear optical responses

order parameters	symmetry-allowed nonlinear conductivities
τ_z	$\sigma_{xx}^x(\omega) = -\sigma_{xy}^y(\omega) = -\sigma_{yx}^y(\omega) = -\sigma_{yy}^x(\omega)$
$\tau_z\sigma_x$	$\sigma_{xx}^x(\omega), \sigma_{xy}^y(\omega), \sigma_{yx}^y(\omega), \sigma_{yy}^x(\omega)$
σ_z	$\sigma_{xx}^x(\omega) = -\sigma_{xy}^y(\omega) = -\sigma_{yx}^y(\omega) = -\sigma_{yy}^x(\omega),$ $\sigma_{xx}^y(\omega) = \sigma_{xy}^x(\omega) = -\sigma_{yx}^x(\omega) = -\sigma_{yy}^y(\omega)$
σ_y	$\sigma_{yy}^y(\omega), \sigma_{xx}^y(\omega), \sigma_{xy}^x(\omega), \sigma_{yx}^x(\omega)$

parameter ($\tau_x\sigma_y, \tau_y\sigma_x$), and a VP state characterized by order parameter τ_z . A VP order actually spontaneously breaks both C_{2z} , time-reversal (\mathcal{T}), and C_{2y} symmetries, and preserves $C_{2z}\mathcal{T}$, C_{3z} , and C_{2x} symmetries. Such a state exhibits an intriguing current pattern in real space consisting of three pairs counter-propagating current loops in the moiré primitive cell, which contribute to staggered orbital magnetic fluxes [33]. Such a state is thus dubbed as a “moiré orbital antiferromagnetic state” [33]. Indeed both C_{2z} and \mathcal{T} symmetries due to such real-space current pattern, which may induce the nonlinear optical response with symmetry-allowed nonlinear optical conductivity components: $\sigma_{xx}^x(\omega) = -\sigma_{xy}^y(\omega) = -\sigma_{yx}^y(\omega) = -\sigma_{yy}^x(\omega)$ [51]. In particular, $\sigma_{xx}^x(\omega)$ is *induced by the valley polarization*, i.e., $\sigma_{xx}^x(\omega) = \sigma_{xx,z}^x(\omega)\langle\tau_z\rangle$ [51]. On the other hand, although the K-IVC order ($\tau_x\sigma_y, \tau_y\sigma_x$) also spontaneously breaks C_{2z} and \mathcal{T} symmetries, it preserves a “Kramers” \mathcal{T} symmetry (\mathcal{T}') [32] with $\mathcal{T}' = \tau_z\mathcal{T}$. In this work we find that the K-IVC order also preserves a “Kramers” C_{2z} symmetry (C'_{2z}), with $C'_{2z} = \tau_z C_{2z}$. The C'_{2z} symmetry forbids any nonlinear optical response. Thus nonlinear optical response can be considered as a unique probe to distinguish the VP and K-IVC states, both of which are featureless insulators in the linear-response regime.

In Table III we list all the four possible order parameters, i.e., τ_z , $\tau_z\sigma_x$, σ_z , and σ_y , that are allowed to have nonzero nonlinear optical responses in TBG. The symmetry-allowed nonlinear optical conductivity tensor $\sigma_{ab}^c(\omega)$ ($a, b, c = x, y$) for these four types of ordered states are also given in Table III.

In order to verify the above argument, we have numerically calculated the SHG susceptibility for various different ordered states in TBG, assuming a constant, \mathbf{k} independent order parameter with amplitude of 1 meV in each state, with the filling fixed at CNP. The results are presented in Fig. 4(a). We see that the nonlinear susceptibilities vanish for both K-IVC state, and the time-reversal invariant intervalley coherent (T-IVC) state characterized by order parameter ($\tau_x\sigma_x, \tau_y\sigma_x$). In contrast, the SHG susceptibility of a VP state is as large as $\pm 800 \mu\text{m}/\text{V}^2$ when $\omega \sim 15 \text{ meV}$, in perfect agreement with previous analysis.

Given that there are substantial valley polarization $\langle\tau_z\rangle$ in the CIs of all of the integer fillings (see Table I), we

have explicitly calculated the SHG susceptibility $\text{Im}\chi_{xx}^x$ of the Hartree-Fock ground states at different integer fillings [51], which are presented in Fig. 4(b). Substantial SHG responses are obtained at all of these fillings, which are the hallmark of nonzero valley polarizations in these CIs. Similar argument applies to the DW states at $\nu = 1, 3, 7/2$ and $8/3$. Since there are nonzero valley polarizations in all of these DW states, non-vanishing SHG and shif-current in the terahertz and infrared frequency regimes are expected.

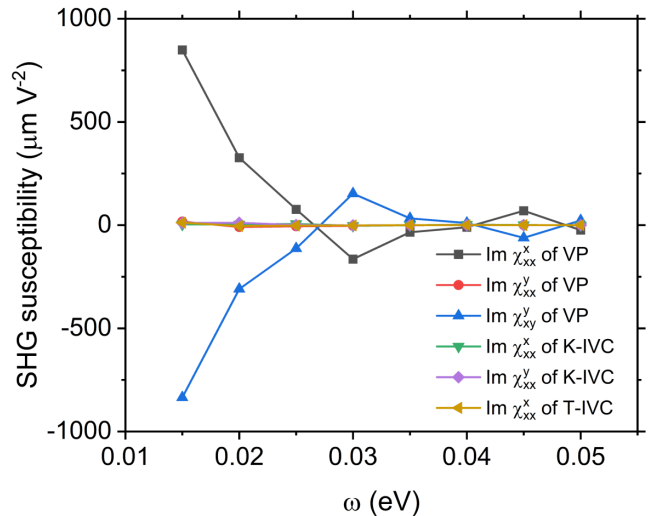


FIG. 4: The nonlinear optical response of TBG at the CNP assuming constant order parameters with amplitudes (1 meV) applied to the flat bands.

Conclusion. — In this work we have theoretically studied the correlated insulators and density wave states at different integer and fractional fillings of the flat bands based on extended unrestricted HF calculations with screening effects treated by cRPA method. We have explained the nature of the recently observed density wave states and symmetry-breaking Chern insulator states at $\nu = 1, 3, 7/2$, and $8/3$ fillings. We also find that most of the CI and DW states exhibit substantial valley polarizations, which would contribute to giant nonlinear optical responses. We have identified the symmetry-allowed nonlinear optical conductivity components in different types of ordered states, and calculated the nonlinear optical responses with different order parameters. Our results indicate the nonlinear optical response may serve as a unique probe to distinguish different types of correlated states observed in magic-angle TBG.

Acknowledgements. — This work is supported by the National Key R & D program of China (grant no. 2020YFA0309601), the National Science Foundation of China (grant no. 12174257), and the start-up grant of ShanghaiTech University. We would like to thank Prof. Xi Dai and Prof. Jian Kang for valuable discussions.

* liujp@shanghaitech.edu.cn

- [1] Y. Cao, V. Fatemi, A. Demir, S. Fang, S. L. Tomarken, J. Y. Luo, J. D. Sanchez-Yamagishi, K. Watanabe, T. Taniguchi, E. Kaxiras, et al., *Nature* **556**, 80 (2018).
- [2] X. Lu, P. Stepanov, W. Yang, M. Xie, M. A. Aamir, I. Das, C. Urgell, K. Watanabe, T. Taniguchi, G. Zhang, et al., *Nature* **574**, 653 (2019).
- [3] A. Kerelsky, L. J. McGilly, D. M. Kennes, L. Xian, M. Yankowitz, S. Chen, K. Watanabe, T. Taniguchi, J. Hone, C. Dean, et al., *Nature* **572**, 95 (2019).
- [4] Y. Jiang, X. Lai, K. Watanabe, T. Taniguchi, K. Haule, J. Mao, and E. Y. Andrei, *Nature (London)* **573**, 91 (2019).
- [5] Y. Xie, B. Lian, B. Jäck, X. Liu, C.-L. Chiu, K. Watanabe, T. Taniguchi, B. A. Bernevig, and A. Yazdani, *Nature (London)* **572**, 101 (2019).
- [6] Y. Choi, J. Kemmer, Y. Peng, A. Thomson, H. Arora, R. Polski, Y. Zhang, H. Ren, J. Alicea, G. Refael, et al., *Nature Physics* pp. 1–7 (2019).
- [7] M. Serlin, C. Tschirhart, H. Polshyn, Y. Zhang, J. Zhu, K. Watanabe, T. Taniguchi, L. Balents, and A. Young, *Science* (2019).
- [8] P. Stepanov, I. Das, X. Lu, A. Fahimniya, K. Watanabe, T. Taniguchi, F. H. L. Koppens, J. Lischner, L. Levitov, and D. K. Efetov, *Nature* **583**, 375 (2020), ISSN 1476-4687.
- [9] Y. Saito, J. Ge, K. Watanabe, T. Taniguchi, and A. F. Young, *Nature Physics* **16**, 926 (2020), ISSN 1745-2481.
- [10] X. Liu, Z. Wang, K. Watanabe, T. Taniguchi, O. Vafek, and J. Li, *Science* **371**, 1261 (2021).
- [11] A. L. Sharpe, E. J. Fox, A. W. Barnard, J. Finney, K. Watanabe, T. Taniguchi, M. A. Kastner, and D. Goldhaber-Gordon, *Science* **365**, 605 (2019).
- [12] P. Stepanov, M. Xie, T. Taniguchi, K. Watanabe, X. Lu, A. H. MacDonald, B. A. Bernevig, and D. K. Efetov (2020), 2012.15126.
- [13] K. P. Nuckolls, M. Oh, D. Wong, B. Lian, K. Watanabe, T. Taniguchi, B. A. Bernevig, and A. Yazdani, *Nature* **588**, 610 (2020).
- [14] S. Wu, Z. Zhang, K. Watanabe, T. Taniguchi, and E. Y. Andrei, *Nature Materials* (2021), ISSN 1476-4660.
- [15] I. Das, X. Lu, J. Herzog-Arbeitman, Z.-D. Song, K. Watanabe, T. Taniguchi, B. A. Bernevig, and D. K. Efetov, *Nature Physics* **17**, 710 (2021).
- [16] A. T. Pierce, Y. Xie, J. M. Park, E. Khalaf, S. H. Lee, Y. Cao, D. E. Parker, P. R. Forrester, S. Chen, K. Watanabe, et al. (2021), 2101.04123.
- [17] J. Liu and X. Dai, *Nature Reviews Physics* **3**, 367 (2021), ISSN 2522-5820.
- [18] Y. Cao, V. Fatemi, S. Fang, K. Watanabe, T. Taniguchi, E. Kaxiras, and P. Jarillo-Herrero, *Nature* **556**, 43 (2018).
- [19] M. Yankowitz, S. Chen, H. Polshyn, Y. Zhang, K. Watanabe, T. Taniguchi, D. Graf, A. F. Young, and C. R. Dean, *Science* **363**, 1059 (2019).
- [20] E. Codecido, Q. Wang, R. Koester, S. Che, H. Tian, R. Lv, S. Tran, K. Watanabe, T. Taniguchi, F. Zhang, et al., *Science Advances* **5** (2019).
- [21] Y. Cao, D. Rodan-Legrain, J. M. Park, N. F. Yuan, K. Watanabe, T. Taniguchi, R. M. Fernandes, L. Fu, and P. Jarillo-Herrero, *science* **372**, 264 (2021).
- [22] R. Bistritzer and A. H. MacDonald, *Proceedings of the National Academy of Sciences* **108**, 12233 (2011).
- [23] Z. Song, Z. Wang, W. Shi, G. Li, C. Fang, and B. A. Bernevig, *Phys. Rev. Lett.* **123**, 036401 (2019).
- [24] J. Ahn, S. Park, and B.-J. Yang, *Phys. Rev. X* **9**, 021013 (2019).
- [25] H. C. Po, L. Zou, T. Senthil, and A. Vishwanath, *Phys. Rev. B* **99**, 195455 (2019).
- [26] G. Tarnopolsky, A. J. Kruchkov, and A. Vishwanath, *Phys. Rev. Lett.* **122**, 106405 (2019).
- [27] J. Liu, J. Liu, and X. Dai, *Phys. Rev. B* **99**, 155415 (2019).
- [28] J. Kang and O. Vafek, *Phys. Rev. Lett.* **122**, 246401 (2019).
- [29] K. Seo, V. N. Kotov, and B. Uchoa, *Phys. Rev. Lett.* **122**, 246402 (2019).
- [30] M. Xie and A. H. MacDonald, *Phys. Rev. Lett.* **124**, 097601 (2020).
- [31] N. Bultinck, S. Chatterjee, and M. P. Zaletel, *Phys. Rev. Lett.* **124**, 166601 (2020).
- [32] N. Bultinck, E. Khalaf, S. Liu, S. Chatterjee, A. Vishwanath, and M. P. Zaletel, *Phys. Rev. X* **10**, 031034 (2020).
- [33] J. Liu and X. Dai, *Phys. Rev. B* **103**, 035427 (2021).
- [34] Y. Zhang, K. Jiang, Z. Wang, and F. Zhang, *Phys. Rev. B* **102**, 035136 (2020).
- [35] K. Hejazi, X. Chen, and L. Balents, *Phys. Rev. Research* **3**, 013242 (2021).
- [36] J. Kang and O. Vafek, *Phys. Rev. B* **102**, 035161 (2020).
- [37] B.-B. Chen, Y. D. Liao, Z. Chen, O. Vafek, J. Kang, W. Li, and Z. Y. Meng, *Nature Communications* **12**, 5480 (2021).
- [38] C. Lu, Y. Zhang, Y. Zhang, M. Zhang, C.-C. Liu, Z.-C. Gu, W.-Q. Chen, and F. Yang, *arXiv preprint arXiv:2003.09513* (2020).
- [39] Y. Da Liao, J. Kang, C. N. Breiør, X. Y. Xu, H.-Q. Wu, B. M. Andersen, R. M. Fernandes, and Z. Y. Meng, *Phys. Rev. X* **11**, 011014 (2021).
- [40] B. A. Bernevig, Z.-D. Song, N. Regnault, and B. Lian, *Phys. Rev. B* **103**, 205413 (2021).
- [41] B. Lian, Z.-D. Song, N. Regnault, D. K. Efetov, A. Yazdani, and B. A. Bernevig, *Phys. Rev. B* **103**, 205414 (2021).
- [42] T. Soejima, D. E. Parker, N. Bultinck, J. Hauschild, and M. P. Zaletel, *Phys. Rev. B* **102**, 205111 (2020).
- [43] P. Potasz, M. Xie, and A. H. MacDonald (2021), 2102.02256.
- [44] X. Zhang, G. Pan, Y. Zhang, J. Kang, and Z. Y. Meng, *Chinese Physics Letters* **38**, 077305 (2021).
- [45] J. S. Hofmann, E. Khalaf, A. Vishwanath, E. Berg, and J. Y. Lee (2021), 2105.12112.
- [46] D. E. Parker, T. Soejima, J. Hauschild, M. P. Zaletel, and N. Bultinck, *Phys. Rev. Lett.* **127**, 027601 (2021).
- [47] H. Polshyn, Y. Zhang, M. A. Kumar, T. Soejima, P. Ledwith, K. Watanabe, T. Taniguchi, A. Vishwanath, M. P. Zaletel, and A. F. Young (2021), 2104.01178.
- [48] Y. Xie, A. T. Pierce, J. M. Park, D. E. Parker, E. Khalaf, P. Ledwith, Y. Cao, S. H. Lee, S. Chen, P. R. Forrester, et al. (2021), 2107.10854.
- [49] Y. H. Kwan, G. Wagner, T. Soejima, M. P. Zaletel, S. H. Simon, S. A. Parameswaran, and N. Bultinck (2021), 2105.05857.
- [50] K. Zhang, Y. Zhang, L. Fu, and E.-A. Kim (2021), 2105.13371.

- [51] See Supplemental Information for: (a) the details for the continuum model of twisted bilayer graphene, (b) the Coulomb interactions and the Hartree-Fock method, (c) screening effects from the remote bands treated by constrained random phase approximation, (d) more results about Hartree-Fock ground states at integer fillings with preserved translational symmetry, (e) more results about the density-wave states, and (f) symmetry analysis on the nonlinear optical response in different ordered phases.
- [52] J. Kang, B. A. Bernevig, and O. Vafek (2021), 2104.01145.
- [53] T. I. Vanhala and L. Pollet, *Phys. Rev. B* **102**, 035154 (2020).
- [54] M. Koshino, N. F. Q. Yuan, T. Koretsune, M. Ochi, K. Kuroki, and L. Fu, *Phys. Rev. X* **8**, 031087 (2018).
- [55] D. Wong, K. P. Nuckolls, M. Oh, B. Lian, Y. Xie, S. Jeon, K. Watanabe, T. Taniguchi, B. A. Bernevig, and A. Yazdani, *Nature* **582**, 198 (2020), ISSN 1476-4687.
- [56] U. Zondiner, A. Rozen, D. Rodan-Legrain, Y. Cao, R. Queiroz, T. Taniguchi, K. Watanabe, Y. Oreg, F. von Oppen, A. Stern, et al., *Nature* **582**, 203 (2020), ISSN 1476-4687.
- [57] J. M. Pizarro, M. Rösner, R. Thomale, R. Valentí, and T. O. Wehling, *Phys. Rev. B* **100**, 161102 (2019).
- [58] J. Rath and A. J. Freeman, *Phys. Rev. B* **11**, 2109 (1975).
-

Supplementary Information for “Correlated insulators, density wave states, and their nonlinear optical response in magic-angle twisted bilayer graphene”

I The continuum model for twisted bilayer graphene

The Bistritzer-Macdonald continuum model is adopted to describe the low-energy physics of twisted bilayer graphene around the magic angle:

$$H_\mu^0(\mathbf{r}) = \begin{pmatrix} -\hbar v_F(\hat{\mathbf{k}} - \mathbf{K}_1^\mu) \cdot \sigma_\mu & U_\mu(\mathbf{r}) \\ U_\mu^\dagger(\mathbf{r}) & -\hbar v_F(\hat{\mathbf{k}} - \mathbf{K}') \cdot \sigma_\mu \end{pmatrix}, \quad (6)$$

where v_F represents the Fermi velocity, $\hat{\mathbf{k}} = -i\nabla$, and $\sigma_\mu = (\mu\sigma_x, \sigma_y)$ denote the Pauli matrix in the sublattice space. Our Hamiltonian is expanded near the Dirac point \mathbf{K}_l^μ ($l = 1, 2$), with $\mu = \mp$ standing for the K/K' valley. The $U_\mu(\mathbf{r})$ matrix refers to the interlayer coupling which introduces a smooth moiré potential,

$$U_\mu(\mathbf{r}) = \begin{pmatrix} u_0 g_\mu(\mathbf{r}) & u'_0 g_\mu(\mathbf{r} - \mu\mathbf{r}_{AB}) \\ u'_0 g_\mu(\mathbf{r} + \mu\mathbf{r}_{AB}) & u_0 g_\mu(\mathbf{r}) \end{pmatrix} e^{i\mu\Delta\mathbf{K}\cdot\mathbf{r}}, \quad (7)$$

where $\mathbf{r}_{AB} = (\sqrt{3}L_s/3, 0)$, u'_0 and u_0 refer to the intersublattice and intrasublattice interlayer tunneling amplitudes, with $u'_0 = 0.0975$ eV, and $u_0 = 0.0797$ eV [54]. u_0 is smaller than u'_0 due to the effects of atomic corrugations. $\Delta\mathbf{K} = \mathbf{K} - \mathbf{K}' = (0, 4\pi/3L_s)$ is the shift between the Dirac points of two layers. We define the phase factor $g(\mathbf{r}) = \sum_{j=1}^3 e^{-i\mu\mathbf{q}_j\cdot\mathbf{r}}$, with $\mathbf{q}_1 = (0, 4\pi/3L_s)$, $\mathbf{q}_2 = (-2\pi/\sqrt{3}L_s, -2\pi/3L_s)$, and $\mathbf{q}_3 = (2\pi/\sqrt{3}L_s, -2\pi/3L_s)$.

The moiré potential $U_M(\mathbf{r})$ preserves the moiré translational symmetry with real-space primitive lattice vectors $\mathbf{R}_1 = (\sqrt{3}L_s/2, -L_s/2)$ and $\mathbf{R}_2 = (\sqrt{3}L_s/2, L_s/2)$, and the corresponding reciprocal vectors are denoted as $\mathbf{g}_1 = (2\pi/(\sqrt{3}L_s), -2\pi/L_s)$ and $\mathbf{g}_2 = (2\pi/(\sqrt{3}L_s), 2\pi/L_s)$. In order to study the density wave states, we consider the possibility that the system spontaneously breaks the moiré translational symmetry forming a doubled moiré supercell and a tripled $\sqrt{3} \times \sqrt{3}$ moiré supercell, where the lattice vectors are denoted by red arrows (doubled cell) and blue arrows (triple cell) in Fig. 1(a) of main text. For a generic case, we consider an enlarged moiré supercell characterized by $\mathbf{R}_1^s = n_{11}\mathbf{R}_1 + n_{12}\mathbf{R}_2$, and $\mathbf{R}_2^s = n_{21}\mathbf{R}_1 + n_{22}\mathbf{R}_2$, where n_{11} , n_{12} , n_{21} , and n_{22} are integers characterizing the enlarged supercell. Then the corresponding moiré reciprocal vectors are expressed as The reciprocal moiré vector is \mathbf{b}_1 and \mathbf{b}_2 , then the reciprocal moiré vector of the M_s -time supercell moiré lattice can be written as

$$\begin{aligned} \mathbf{G}_1 &= (n_{22}\mathbf{b}_1 - n_{21}\mathbf{b}_2)/N_c, \\ \mathbf{G}_2 &= (n_{11}\mathbf{b}_2 - n_{12}\mathbf{b}_1)/N_c, \end{aligned} \quad (8)$$

where $N_c = n_{11}n_{22} - n_{12}n_{21}$ (we take the convention that $N_c > 0$) denotes the ratio between the area of the enlarged moiré supercell and the primitive moiré cell. To be specific, $n_{11} = n_{22} = 1$ and $n_{12} = n_{21} = 0$ refer to the primitive moiré cell of TBG. If $n_{11} = n_{22} = n_{12} = -n_{21} = 1$, this group of indices represent the doubled moiré supercell. The tripled $\sqrt{3} \times \sqrt{3}$ moiré supercell is characterized by $n_{11} = n_{12} = -n_{21} = 1$ and $n_{22} = 2$. The inverse of Eq. (8) reads

$$\begin{aligned} \mathbf{g}_1 &= n_{11}\mathbf{G}_1 + n_{21}\mathbf{G}_2, \\ \mathbf{g}_2 &= n_{12}\mathbf{G}_1 + n_{22}\mathbf{G}_2. \end{aligned} \quad (9)$$

We have performed Hartree-Fock calculations for primitive, doubled, and tripled moiré supercells, using the expressions of the reciprocal vectors given in Eqs. (8)-(9).

II The Hartree-Fock method and remote-band potentials

The inter-site Coulomb interactions in the TBG system is expressed as,

$$H_C = \frac{1}{2N_s} \sum_{\alpha\alpha'} \sum_{\mathbf{k}\mathbf{k}'} \sum_{\sigma\sigma'} V(\mathbf{q}) \hat{c}_{\mathbf{k}+\mathbf{q},\alpha\sigma}^\dagger \hat{c}_{\mathbf{k}'-\mathbf{q},\alpha'\sigma'}^\dagger \hat{c}_{\mathbf{k}',\alpha'\sigma'} \hat{c}_{\mathbf{k},\alpha\sigma} \quad (10)$$

where \mathbf{k} and \mathbf{q} represent atomic wavevectors defined in the Brillouin zone of graphene. The layer and sublattice indices are denoted by α , and σ refers to the spin index. The $\hat{c}_{\mathbf{k},\alpha\sigma}$ and $\hat{c}_{\mathbf{k},\alpha\sigma}^\dagger$ refer to the electron annihilation and

creation operators. One can further expand the wavevectors around the Dirac points, which distinguish the Coulomb interaction into an intravalley part and an intervalley part, where the dominant intra-valley Coulomb interaction is expressed as,

$$H_C^{\text{intra}} = \frac{1}{2N_s} \sum_{\alpha\alpha'} \sum_{\mu\mu',\sigma\sigma'} \sum_{\mathbf{k}\mathbf{k}'\mathbf{q}} V(\mathbf{q}) \hat{c}_{\mu\sigma\alpha,\mathbf{k}+\mathbf{q}}^\dagger \hat{c}_{\mu'\sigma'\alpha',\mathbf{k}'-\mathbf{q}}^\dagger \hat{c}_{\mu'\sigma'\alpha',\mathbf{k}'} \hat{c}_{\mu\sigma\alpha,\mathbf{k}}, \quad (11)$$

where $\mu, \mu' = \pm$ denote the valley indices. The double-gate screened Coulomb interaction

$$V(\mathbf{q}) = \frac{e^2 \tanh(|\mathbf{q}|d_s)}{2\Omega_M \epsilon \epsilon_0 |\mathbf{q}|} \quad (12)$$

in which Ω_M is the area of moiré supercell, d_s is the screening length 400Å and $\epsilon_{\text{BN}} = 4$ refers to the dielectric constant of the hexagonal boron nitride substrates.

We further transform the original basis to the band basis

$$\hat{c}_{\mu\alpha\sigma,\mathbf{k}} = \sum_n C_{\mu\alpha\mathbf{G},n}(\tilde{\mathbf{k}}) \hat{c}_{\mu\sigma,n\tilde{\mathbf{k}}}, \quad (13)$$

in which $C_{\mu\alpha\mathbf{G},n}(\tilde{\mathbf{k}})$ is the wavefunction coefficient of the n th Bloch eigenstate at $\tilde{\mathbf{k}}$ of valley μ : $|\psi_{n\tilde{\mathbf{k}}\mu}\rangle = \sum_{\alpha\mathbf{G}} C_{\mu\alpha\mathbf{G},n}(\tilde{\mathbf{k}})|\mu\alpha,\mathbf{G} + \tilde{\mathbf{k}}\rangle$, with \mathbf{G} denoting the reciprocal vector. Under this transformation, the intra-valley Coulomb interaction can be written as

$$H^{\text{intra}} = \frac{1}{2N_s} \sum_{\tilde{\mathbf{k}}\tilde{\mathbf{k}}'\tilde{\mathbf{q}}} \sum_{\mu\mu',\sigma\sigma'} \sum_{nm,n'm'} \left(\sum_{\mathbf{Q}} V(\mathbf{Q} + \tilde{\mathbf{q}}) \Omega_{nm,n'm'}^{\mu\sigma,\mu'\sigma'}(\tilde{\mathbf{k}}, \tilde{\mathbf{k}}', \tilde{\mathbf{q}}, \mathbf{Q}) \right) \hat{c}_{\mu\sigma,n\tilde{\mathbf{k}}+\tilde{\mathbf{q}}}^\dagger \hat{c}_{\mu'\sigma',n'\tilde{\mathbf{k}}'-\tilde{\mathbf{q}}}^\dagger \hat{c}_{\mu'\sigma',m'\tilde{\mathbf{k}}'} \hat{c}_{\mu\sigma,m\tilde{\mathbf{k}}} \quad (14)$$

in which the form factor $\Omega_{nm,n'm'}^{\mu\sigma,\mu'\sigma'}$ is written as

$$\Omega_{nm,n'm'}^{\mu\sigma,\mu'\sigma'}(\tilde{\mathbf{k}}, \tilde{\mathbf{k}}', \tilde{\mathbf{q}}, \mathbf{Q}) = \sum_{\alpha\alpha'\mathbf{G}\mathbf{G}'} C_{\mu\sigma\alpha\mathbf{G}+\mathbf{Q},n\tilde{\mathbf{k}}+\tilde{\mathbf{q}}}^* C_{\mu'\sigma'\alpha'\mathbf{G}'-\mathbf{Q},n'\tilde{\mathbf{k}}'-\tilde{\mathbf{q}}} C_{\mu'\sigma'\alpha'\mathbf{G}',m'\tilde{\mathbf{k}}'} C_{\mu\sigma\alpha\mathbf{G},m\tilde{\mathbf{k}}} \quad (15)$$

Here the wavevector \mathbf{q} is decomposed as $\mathbf{q} = \mathbf{Q} + \tilde{\mathbf{q}}$, $\mathbf{k} = \mathbf{G} + \tilde{\mathbf{k}}$ where \mathbf{G} or \mathbf{Q} is a moiré reciprocal vector and $\tilde{\mathbf{k}}$ or $\tilde{\mathbf{q}}$ remarks the wavevector in the moiré Brillouin zone. When we perform extended Hartree-Fock calculations for the moiré superlattices with doubled or tripled primitive cells, \mathbf{G} in the above equation refers to the moiré reciprocal vectors of the enlarged supercell, $\tilde{\mathbf{k}}$ or $\tilde{\mathbf{q}}$ refers to a wavevector in the folded moiré Brillouin zone, as shown in Fig. 1(b) of main text.

Since intravalley Coulomb interactions are the leading ones in TBG, from now on we only consider the intravalley Coulomb interaction under band basis. We make Hartree-Fock approximation to Eq. (14) to decompose the two-particle interactions into a superposition of the Hartree and Fock mean-field single-particle Hamiltonians, where the Hartree term is expressed as

$$H_H^{\text{intra}} = \frac{1}{2N_s} \sum_{\tilde{\mathbf{k}}\tilde{\mathbf{k}}'} \sum_{\mu\mu',\sigma\sigma'} \sum_{nm,n'm'} \left(\sum_{\mathbf{Q}} V(\mathbf{Q}) \Omega_{nm,n'm'}^{\mu\sigma,\mu'\sigma'}(\tilde{\mathbf{k}}, \tilde{\mathbf{k}}', 0, \mathbf{Q}) \right) \times \left(\langle \hat{c}_{\mu\sigma,n\tilde{\mathbf{k}}}^\dagger \hat{c}_{\mu\sigma,m\tilde{\mathbf{k}}} \rangle \hat{c}_{\mu'\sigma',n'\tilde{\mathbf{k}}'}^\dagger \hat{c}_{\mu'\sigma',m'\tilde{\mathbf{k}}'} + \langle \hat{c}_{\mu'\sigma',n'\tilde{\mathbf{k}}'}^\dagger \hat{c}_{\mu'\sigma',m'\tilde{\mathbf{k}}'} \rangle \hat{c}_{\mu\sigma,n\tilde{\mathbf{k}}}^\dagger \hat{c}_{\mu\sigma,m\tilde{\mathbf{k}}} \right) \quad (16)$$

and the Fock term is

$$H_F^{\text{intra}} = -\frac{1}{2N_s} \sum_{\tilde{\mathbf{k}}\tilde{\mathbf{k}}'} \sum_{\mu\mu',\sigma\sigma'} \sum_{nm,n'm'} \left(\sum_{\mathbf{Q}} V(\tilde{\mathbf{k}}' - \tilde{\mathbf{k}} + \mathbf{Q}) \Omega_{nm,n'm'}^{\mu\sigma,\mu'\sigma'}(\tilde{\mathbf{k}}, \tilde{\mathbf{k}}', \tilde{\mathbf{k}}' - \tilde{\mathbf{k}}, \mathbf{Q}) \right) \times \left(\langle \hat{c}_{\mu\sigma,n\tilde{\mathbf{k}}}^\dagger \hat{c}_{\mu'\sigma',m'\tilde{\mathbf{k}}'} \rangle \hat{c}_{\mu'\sigma',n'\tilde{\mathbf{k}}'}^\dagger \hat{c}_{\mu\sigma,m\tilde{\mathbf{k}}} + \langle \hat{c}_{\mu'\sigma',n'\tilde{\mathbf{k}}'}^\dagger \hat{c}_{\mu\sigma,m\tilde{\mathbf{k}}} \rangle \hat{c}_{\mu\sigma,n\tilde{\mathbf{k}}}^\dagger \hat{c}_{\mu'\sigma',m'\tilde{\mathbf{k}}'} \right). \quad (17)$$

We further project the interaction Hamiltonian (with Hartree-Fock approximations) onto the flat-band subspace. However, the treatment of the remote bands is very tricky when making such a projection. Since the remote bands

below the charge neutrality point (CNP) are all occupied, which can interact with the electrons occupying the flat bands, and such interactions are pointed out to be important in determining the ground states and low-energy excitations in magic-angle TBG [40, 41, 52]. In particular, in Ref. 40, it is proposed that one can conveniently write the interaction as

$$H'_C = \frac{N_s}{2} \sum_{\mathbf{q}} V(\mathbf{q}) \delta\hat{\rho}(\mathbf{q}) \delta\hat{\rho}(-\mathbf{q}), \quad (18)$$

where $\delta\hat{\rho}(\mathbf{q}) = \delta\hat{\rho}(\tilde{\mathbf{q}} + \mathbf{Q})$ is defined as

$$\delta\hat{\rho}(\mathbf{q}) = \frac{1}{N_s} \sum_{\tilde{\mathbf{k}}} \sum_{\mu\sigma\alpha\mathbf{G}} \left(\hat{c}_{\mu\sigma\alpha, \mathbf{G} + \mathbf{Q} + \tilde{\mathbf{k}} + \tilde{\mathbf{q}}}^\dagger \hat{c}_{\mu\sigma\alpha, \mathbf{G} + \tilde{\mathbf{k}}} - (1/2) \delta_{\tilde{\mathbf{q}}, \mathbf{0}} \delta_{\tilde{\mathbf{Q}}, \mathbf{0}} \right). \quad (19)$$

Again, the μ , σ , and α indices refer to the valley, spin, and layer/sublattice indices respectively. \mathbf{G} or \mathbf{Q} denotes to a moiré reciprocal vector and $\tilde{\mathbf{k}}$ or $\tilde{\mathbf{q}}$ denotes a wavevector within the moiré Brillouin zone. In the case of doubled or tripled moiré supercell, \mathbf{G} and \mathbf{Q} would correspond to the reciprocal vectors of the enlarged moiré supercells, and $\tilde{\mathbf{k}}$ and $\tilde{\mathbf{q}}$ are wavevectors within the folded moiré Brillouin zone as shown in Fig. 1(b) of main text.

Note that if the full Hilbert space is included, then Eq. (18) is equivalent to the normal-ordered interaction (Eq. (11)) up to a constant chemical potential term. However, if the interaction is projected onto the flat bands, the Hamiltonian in Eq. (18) becomes different from the normal-ordered one. It turns out that if one makes Hartree-Fock approximations, then the remote-band Hartree-Fock potential acted on the flat bands is exactly the difference between Eq. (18) and the normal-ordered one by virtue of the $C_{2z}\mathcal{T}$ symmetry and a particle-hole symmetry of the continuum model [40]. To be specific, the remote-band Hartree-Fock potential can be expressed in band basis as:

$$\begin{aligned} \Delta H_I = & -\frac{1}{2N_s} \sum_{\mathbf{k}\mu s} \sum_{nm} \left(\sum_{\mathbf{Q}} V(\mathbf{Q}) \sum_{\substack{\tilde{\mathbf{k}}\mu' \\ n's'}} \Omega_{nm, n'n'}^{\mu, \mu'}(\tilde{\mathbf{k}}, \tilde{\mathbf{k}}', 0, \mathbf{Q}) \right) \hat{c}_{\mu s, n\tilde{\mathbf{k}}}^\dagger \hat{c}_{\mu s, m\tilde{\mathbf{k}}} \\ & + \frac{1}{2N_s} \sum_{\mathbf{k}\mu s} \sum_{nm} \left(\sum_{\mathbf{Q}\tilde{\mathbf{q}}} V(\mathbf{Q} + \tilde{\mathbf{q}}) \sum_{n'} \Omega_{nn', n'm}^{\mu, \mu'}(\tilde{\mathbf{k}} - \tilde{\mathbf{q}}, \tilde{\mathbf{k}}, \tilde{\mathbf{q}}, \mathbf{Q}) \right) \hat{c}_{\mu s, n\tilde{\mathbf{k}}}^\dagger \hat{c}_{\mu s, m\tilde{\mathbf{k}}} \end{aligned} \quad (20)$$

where the summations of the band indices n, m, n' , and m' are restricted to the flat-band subspace. In our calculations, the Coulomb interactions are projected onto the two flat bands per spin per valley, and the remote-band Hartree-Fock potentials given in Eq. (20) have been included in our calculations.

III The screening effects and constraint RPA method

In the previous definition of Coulomb interactions (Eq. (11)), a double-gate screened interaction has been considered as shown in Eq. (12), in which only the screening effects from the top and bottom metallic gates have been included. The gate-screened Coulomb interactions are further projected onto the flat bands of the TBG system. In reality, the Coulomb interaction between two electrons occupying the flat bands can also be screened due to the virtual excitations of particle-hole pairs from the remote bands. We characterize such screening effects using the constrained random phase approximation (cRPA). In particular, in the flat-band subspace, the Coulomb interaction including such screening effects is expressed as

$$H_{int}^{\text{cRPA}} = \frac{1}{2N_s} \sum_{\tilde{\mathbf{k}}\mu s} \sum_{\tilde{\mathbf{k}}'\mu' s'} \sum_{\substack{\mu, \mu' \\ \sigma, \sigma'}} \sum_{\substack{nn' \\ mm'}} V^{\text{cRPA}}(\tilde{\mathbf{q}})_{\tilde{\mathbf{k}}\mu nm, \tilde{\mathbf{k}}'\mu' n'm'} \hat{c}_{\mu\sigma, n\tilde{\mathbf{k}} + \tilde{\mathbf{q}}}^\dagger \hat{c}_{\mu'\sigma', n'\tilde{\mathbf{k}}' + \tilde{\mathbf{q}}}^\dagger \hat{c}_{\mu'\sigma', m'\tilde{\mathbf{k}}' + \tilde{\mathbf{q}}} \hat{c}_{\mu\sigma, m\tilde{\mathbf{k}}} \quad (21)$$

in which the cRPA screened interaction in the flat-band basis $V^{\text{cRPA}}(\tilde{\mathbf{q}})_{\tilde{\mathbf{k}}\mu nm, \tilde{\mathbf{k}}'\mu' n'm'}$ is expressed as

$$V^{\text{cRPA}}(\tilde{\mathbf{q}})_{\tilde{\mathbf{k}}\mu nm, \tilde{\mathbf{k}}'\mu' n'm'} = \sum_{\mathbf{Q}, \mathbf{Q}'} \lambda_{\tilde{\mathbf{k}}\mu nm, \mathbf{Q}}(\tilde{\mathbf{q}}) V(\tilde{\mathbf{q}})_{\mathbf{Q}, \mathbf{Q}'} \lambda_{\mathbf{Q}', \tilde{\mathbf{k}}'\mu' n'm'}^\dagger, \quad (22)$$

where $\lambda_{\tilde{\mathbf{k}}\mu n m, \mathbf{Q}}$ is defined as

$$\lambda_{\tilde{\mathbf{k}}\mu n m, \mathbf{Q}}(\tilde{\mathbf{q}}) = \sum_{\alpha \mathbf{G}} C_{\mu \alpha \mathbf{G} + \mathbf{Q}, n}^* (\tilde{\mathbf{k}} + \tilde{\mathbf{q}}) C_{\mu \alpha \mathbf{G}, m}(\tilde{\mathbf{k}}) \quad (23)$$

The cRPA screened Coulomb interaction in the band basis $V^{\text{cRPA}}(\tilde{\mathbf{q}})_{\mathbf{Q}, \mathbf{Q}'}$ is expressed as

$$\begin{aligned} V_{\tilde{\mathbf{k}}\mu n m, \tilde{\mathbf{k}}'\mu' m' n'}^{\text{cRPA}}(\tilde{\mathbf{q}}) &= V_{\tilde{\mathbf{k}}\mu n m, \tilde{\mathbf{k}}'\mu' m' n'}(\tilde{\mathbf{q}}) - \frac{2}{N_s} \sum_{n_1 m_1} \sum_{\tilde{\mathbf{k}}_1 \mu_1} V_{\tilde{\mathbf{k}}\mu n m, \tilde{\mathbf{k}}_1 \mu_1 m_1 n_1}(\tilde{\mathbf{q}}) \chi_{\tilde{\mathbf{k}}_1 \mu_1 m_1 n_1}^0(\tilde{\mathbf{q}}) V_{\tilde{\mathbf{k}}_1 \mu_1 m_1 n_1, \tilde{\mathbf{k}}'\mu' m' n'}(\tilde{\mathbf{q}}) \\ &+ \left(\frac{-2}{N_s}\right)^2 \sum_{\substack{n_1 m_1 \\ n_2 m_2}} \sum_{\mu_1 \mu_2} \sum_{\tilde{\mathbf{k}}_1 \tilde{\mathbf{k}}_2} V_{\tilde{\mathbf{k}}\mu n m, \tilde{\mathbf{k}}_1 \mu_1 m_1 n_1}(\tilde{\mathbf{q}}) \chi_{\tilde{\mathbf{k}}_1 \mu_1 m_1 n_1}^0(\tilde{\mathbf{q}}) V_{\tilde{\mathbf{k}}_1 \mu_1 m_1 n_1, \tilde{\mathbf{k}}_2 \mu_2 m_2 n_2}(\tilde{\mathbf{q}}) \chi_{\tilde{\mathbf{k}}_2 \mu_2 m_2 n_2}^0(\tilde{\mathbf{q}}) V_{\tilde{\mathbf{k}}_2 \mu_2 m_2 n_2, \tilde{\mathbf{k}}'\mu' m' n'}(\tilde{\mathbf{q}}) + \dots, \end{aligned} \quad (24)$$

where $V_{\tilde{\mathbf{k}}\mu n m, \tilde{\mathbf{k}}'\mu' m' n'}(\tilde{\mathbf{q}})$ is the double-gate screened Coulomb interaction projected onto the flat bands, i.e., $V_{\tilde{\mathbf{k}}\mu n m, \tilde{\mathbf{k}}'\mu' m' n'}(\tilde{\mathbf{q}}) = \sum_{\mathbf{Q}} V(\mathbf{Q} + \tilde{\mathbf{q}}) \Omega_{nm, n'm'}^{\mu, \mu'}(\tilde{\mathbf{k}}, \tilde{\mathbf{k}}', \tilde{\mathbf{q}}, \mathbf{Q})$, as shown in Eq. (14). The band indices m, m', n, n' refer to the flat-band indices. However, the summation over band indices $\sum'_{n_1 m_1}$ with a superscript $'$ means that the band summation is restricted: n_1 and m_1 cannot be both the flat band indices. In other words, we consider the screening effects to the flat-band electrons from the virtual excitations of particle-hole pairs through the following three processes: the particle-hole pairs are excited (i) from the remote bands below CNP to those above CNP, (ii) from remote bands below CNP to the flat bands, and (iii) from the flat bands to remote bands above CNP. We exclude the particle-hole excitations within the flat-band subspace. This is called the constrained random phase approximation [53, 57].

The static bare susceptibility in the band basis is expressed as

$$\chi_{\tilde{\mathbf{k}}\mu m n}^0(\tilde{\mathbf{q}}) = \frac{f(E_{\mu, m\tilde{\mathbf{k}}+\tilde{\mathbf{q}}}) - f(E_{\mu, n\tilde{\mathbf{k}}})}{E_{\mu, n\tilde{\mathbf{k}}} - E_{\mu, m\tilde{\mathbf{k}}+\tilde{\mathbf{q}}}} \quad (25)$$

One can also define the bare susceptibility in the basis of the transferred reciprocal vectors

$$\chi^0(\tilde{\mathbf{q}})_{\mathbf{Q}_1, \mathbf{Q}_2} = \frac{2}{N_s} \sum_{\tilde{\mathbf{k}}_1} \sum_{\mu_1 m_1 n_1} \lambda^\dagger(\tilde{\mathbf{q}})_{\mathbf{Q}_1, \tilde{\mathbf{k}}_1 \mu_1 m_1 n_1} \chi_{\tilde{\mathbf{k}}_1 \mu_1 m_1 n_1}^0(\tilde{\mathbf{q}}) \lambda(\tilde{\mathbf{q}})_{\tilde{\mathbf{k}}_1 \mu_1 m_1 n_1, \mathbf{Q}_2}. \quad (26)$$

It should be noted that the summation over $\tilde{\mathbf{k}}$ can be difficult to converge when there is any van Hove singularity in the energy bands, therefore we have adopted the analytic linear interpolation method [58] to perform the summation of $\tilde{\mathbf{k}}$ points. Then the cRPA screened Coulomb interaction can be re-written as:

$$V_{\tilde{\mathbf{k}}\mu n m, \tilde{\mathbf{k}}'\mu' m' n'}^{\text{cRPA}}(\tilde{\mathbf{q}}) = \sum_{\mathbf{Q}, \mathbf{Q}'} \lambda_{\tilde{\mathbf{k}}\mu n m, \mathbf{Q}}(\tilde{\mathbf{q}}) \left[\hat{V}(\tilde{\mathbf{q}}) \cdot \left(1 + \chi^0(\tilde{\mathbf{q}}) \cdot \hat{V}(\tilde{\mathbf{q}}) \right)^{-1} \right]_{\mathbf{Q}, \mathbf{Q}'} \lambda_{\mathbf{Q}', \tilde{\mathbf{k}}'\mu' m' n'}^\dagger(\tilde{\mathbf{q}}). \quad (27)$$

In the above equation, the double-gate screened Coulomb interaction $V(\mathbf{q}) = V(\tilde{\mathbf{q}} + \mathbf{Q})$ (Eq. (12)) is written in matrix form: $\hat{V}(\tilde{\mathbf{q}})_{\mathbf{Q}, \mathbf{Q}'} = V(\tilde{\mathbf{q}} + \mathbf{Q}) \delta_{\mathbf{Q}, \mathbf{Q}'}$, and we define the dielectric matrix

$$\hat{\epsilon}_{\mathbf{Q}, \mathbf{Q}'}(\tilde{\mathbf{q}}) = \left(1 + \chi^0(\tilde{\mathbf{q}}) \cdot \hat{V}(\tilde{\mathbf{q}}) \right)_{\mathbf{Q}, \mathbf{Q}'} \quad (28)$$

The dielectric function $\epsilon(\tilde{\mathbf{q}} + \mathbf{Q})$ is defined as the dominant diagonal element of Eq. (28), and $\epsilon(\tilde{\mathbf{q}} + \mathbf{Q}) \times \epsilon_{\text{BN}}$ ($\epsilon_{\text{BN}} = 4$) is plotted in Fig. 1(e) of main text. Then, the cRPA screened Coulomb interaction is expressed as

$$\bar{V}^{\text{cRPA}}(\tilde{\mathbf{q}}) = \hat{V}(\tilde{\mathbf{q}}) \cdot (\hat{\epsilon}(\tilde{\mathbf{q}}))^{-1} \quad (29)$$

We further project the cRPA screened Coulomb interactions onto the flat bands, as expressed in Eq. (27). After making Hartree-Fock approximations, the interaction Hamiltonian is decomposed into Hartree and Fock terms as shown in Eqs. (16)-(17). We take $V_{\tilde{\mathbf{k}}\mu n m, \tilde{\mathbf{k}}'\mu' m' n'}^{\text{cRPA}}(\tilde{\mathbf{q}} = \mathbf{0})$ in the Hartree term, and we let $V(\mathbf{k}' - \mathbf{k} + \mathbf{Q}) \rightarrow V(\mathbf{k}' - \mathbf{k} + \mathbf{Q})/\epsilon(\mathbf{k}' - \mathbf{k} + \mathbf{Q})$ in the Fock term, where $V(\mathbf{q})$ is the double-gate screened Coulomb interaction (without the remote-band screening effects) given in Eq. (12).

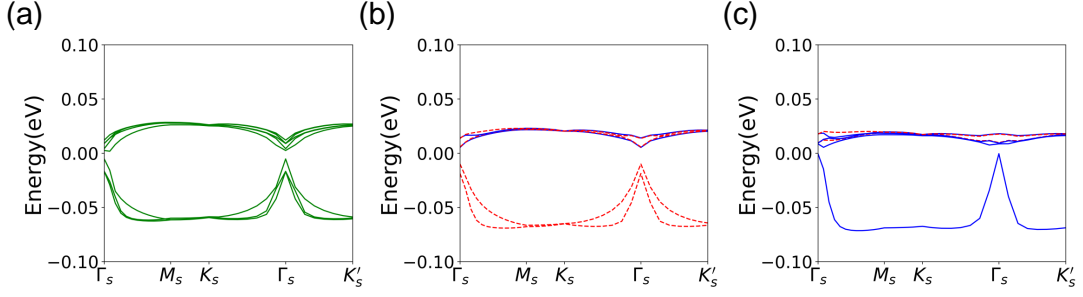


FIG. 5: The Hartree-Fock energy bands of twisted bilayer graphene with $\theta = 1.05^\circ$, at the fillings (a) $\nu = -1$, (b) $\nu = -2$, and (c) $\nu = -3$, where the screening effects from the remote bands and the remote-band Hartree-Fock potentials acted on the flat bands are involved. At the filling $\nu = -2$ and $\nu = -3$, the ground states are spin-valley polarized, thus the energy bands from two valley are marked with blue solid lines and red dash lines.

IV More Hartree-Fock results at integer fillings with preserved moiré translational symmetry

In this section, we show the Hartree-Fock energy bands at the negative integer fillings $\nu = -3, -2, -1$ preserving moiré translational symmetry. The correlated state at the $\nu = -1$ filling is Kramers intervalley coherent (K-IVC) state mixed with some valley polarization $\langle \tau_z \rangle = 1.14$. Such a state at $\nu = -1$ can be intuitively interpreted as follows: two occupied Chern bands from the two valleys with opposite Chern numbers ± 1 are coupled and trivialized by the K-IVC order, leaving one Chern band being occupied, thus the total Chern number is ± 1 . The states at the $\nu = -2$ and $\nu = -3$ fillings become fully spin-valley-polarized phase, with Chern number 0 and -1 respectively.

We introduce a parameter $0 \leq \lambda \leq 1$ to characterize the bandwidth of flat bands in the continuum model. When $\lambda = 0$, the kinetic energy is zero, which is called the flat-band limit. In the following, we will discuss about the ground states under different u_0 and λ parameters at the CNP and $\nu = 2$ filling.

At the CNP, in the chiral limit ($u_0 = 0$) and flat-band limit ($\lambda = 0$), the ground state are highly degenerate due to the $U(4) \times U(4)$ symmetry of the interaction Hamiltonian [32, 40]. If we stay at the flat-band limit and increase u_0 to break the chiral symmetry, the ground states will because the degenerate states of pure valley polarized (VP) state and K-IVC state, by virtue of a $U(4)$ symmetry (including spin degrees of freedom) in the case of non-chiral flat limit [40]. Then in the non-chiral case, further increasing λ (bandwidth) will lift up the energy of the VP state and make the K-IVC mixed with small VP component being the unique ground state as shown in the Fig. 6. In summary, finite bandwidth of flat bands will lift up the energy of a pure VP state, and the breaking of chiral symmetry would induce a mild mixture of the VP order into the K-IVC state.

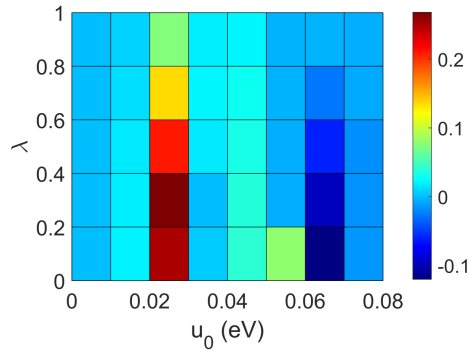


FIG. 6: The normalized valley polarization component $\langle \tau_z \rangle / \langle \tau_z \rangle_{\text{VP}}$ in the K-IVC state at the CNP in which $\langle \tau_z \rangle_{\text{VP}}$ is the valley polarization of pure valley-polarized state at the same parameter point. λ represents the bandwidth of flat bands, and $\lambda = 1$ corresponds to the realistic bandwidth. In the chiral limit, the calculated K-IVC states are all pure K-IVC phases without valley polarization.

As for the ground state at the $\nu = 2$, we show the energy difference between spin-valley polarized (SVP) phase and intervalley coherent (IVC) phase $\Delta E = E_{\text{SVP}} - E_{\text{IVC}}$ with both constant screening $\epsilon = 10$ and with the cRPA method

in Fig. 7(a) and (b). Here the IVC phase can involve both the K-IVC and time-reversal invariant IVC (T-IVC) phase, which are characterized by $(\tau_x\sigma_y, \tau_y\sigma_y)$ and $(\tau_x\sigma_x, \tau_y\sigma_x)$ respectively. With a fixed dielectric constant $\epsilon = 10$, the HF ground states at $\nu=2$ with realistic parameters ($u_0=0.0797$ eV and $\lambda=1$) involve three nearly degenerate states: the IVC state mixed with slight valley and sublattice polarizations ($\tau_i\sigma_j, \tau_z, \sigma_z, i = x, y$), a valley-sublattice polarized state (with order parameters $\tau_z, \sigma_z, \tau_z\sigma_z$), and a spin-sublattice polarized state (with order parameters $s_z, \tau_z\sigma_z, \tau_zs_z\sigma_z$). The energy difference between these states are no more than 10 *mueV*.

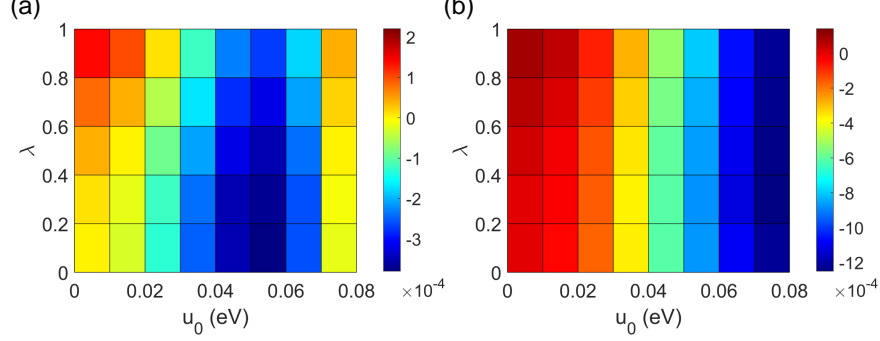


FIG. 7: The energy different between SVP phase and IVC phase $\Delta E = E_{SVP} - E_{IVC}$ with constant screening $\epsilon=10$ (a) and with cRPA method (b). The unit of energies are eV here.

V More HF results about the density wave states

As shown in Fig 8 (a,b), at the filling $\nu=7/2$, there are two degenerate states of K-IVC and SVP state. And these two DW states within double supercell moiré lattice all break the C_{3z} rotational symmetry. The Hartree-Fock band structures of these two states at $nu = 7/2$ are shown in Fig. 8(a) (for SVP state) and (b) (for K-IVC state). The SVP state at $7/2$ filling has a Chern number of 1, while the K-IVC state has a Chern number zero. Thus the K-IVC state at $7/2$ filling is likely the experimentally observed insulator state reported in Ref. 48.

To analyze the symmetry of correlated state at $\nu = 3$ with doubled moiré supercell, in the Fig. 8 we also show the distribution of valley polarization τ_z in the moiré Brillouin zone filling $\nu = 3$. We can see the obvious broken C_{3z} rotational symmetry.

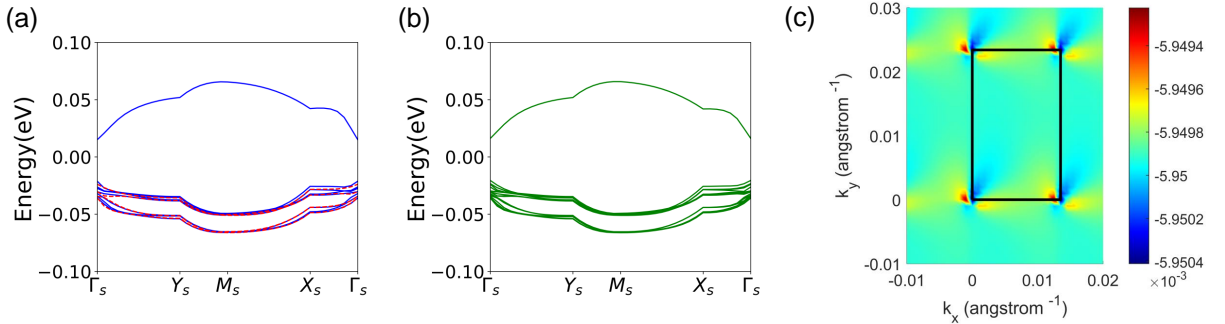


FIG. 8: The Hartree-Fock energy bands of 1.05° -twisted bilayer graphene at the fillings $\nu=7/2$ (a) (SVP phase), $\nu=7/2$ (b) (K-IVC phase). The green lines represent the K-IVC state. In the spin-valley-polarized phase, the energy bands from two valley are remarked with blue solid lines and red dash lines. We also show the distribution of τ_z in the reciprocal space at the filling $\nu=3$.

VI The symmetric analysis about the nonlinear optical response

The nonlinear optical response can be characterized by the second order optical conductivity as

$$j^c(\omega_1 + \omega_2) = \sum_{a,b} \sigma_{ab}^c(\omega_1 + \omega_2)(\omega_1 + \omega_2)E^a(\omega_1)E^b(\omega_2). \quad (30)$$

where $j^c(\omega_1 + \omega_2)$ denotes the photo current density with frequency $\omega_1 + \omega_2$, $E^a(\omega_1)$ and $E^b(\omega_2)$ denote the electric fields with frequency ω_1 and ω_2 , and $a, b, c = x, y$ for 2D systems. $\sigma_{ab}^c(\omega_1, \omega_2)$ is the frequency dependent second-order photo conductivity. In this work we consider two kinds of nonlinear optical responses: the second-harmonic generation (SHG), with $\omega_1 = \omega_2 = \omega$, and the shift-current generation with $\omega_1 = -\omega_2 = \omega$. In the SHG process, the frequency dependent second-order susceptibility is related to the photo conductivity via $\chi_{ab}^c(\omega) = 2i\omega\sigma_{ab}^c(\omega)$, where ω is the frequency of the incident light.

The second-order photo-conductivity in the TBG system can be decomposed into two components: an intrinsic component $\sigma_{ab,0}^c$ that results from the structural C_{2z} symmetry breaking, say, due to hBN alignment; and another component that is induced by the order parameter denoted by \mathcal{N} , which can be expressed as $\sum_d \sigma_{ab,d}^c \mathcal{N}_d$ where \mathcal{N}_d is the d th component of the order parameter. Including both the intrinsic contribution and the order-parameter contribution, the second-order photo conductivity can be written as

$$\sigma_{ab}^c(\omega) = \sigma_{ab,0}^c(\omega) + \sum_d \sigma_{ab,d}^c(\omega) \mathcal{N}_d. \quad (31)$$

An order parameter \mathcal{N} is transformed by a symmetry operation g as: $\mathcal{N}_d \rightarrow \sum_{d'} (\gamma(g))_{dd'} \mathcal{N}_{d'}$, where $\gamma(g)_{dd'}$ is the matrix element of the symmetry operator g represented by the order parameter. Now we make this symmetry transformation on both sides of Eq. (30),

$$\sum_{c'} O(g)_{cc'} j^{c'} = \sum_{ab} \sum_{a'b'} \sigma_{ab,0}^c O(g)_{aa'} E^{a'} O(g)_{bb'} E^{b'} + \sum_{ab} \sum_{a'b'} \sum_{d'} \sigma_{ab,d}^c O(g)_{aa'} O(g)_{bb'} \gamma(g)_{dd'} E^{a'} E^{b'} \mathcal{N}_{d'}. \quad (32)$$

Here $O(g)$ is symmetry representation in Cartesian coordinates. From the above equation, we obtain the constraint on the nonlinear photo conductivity σ_{ab}^c from symmetry g :

$$\begin{aligned} \sum_{abc} O^T(g)_{c_0c} \sigma_{ab,0}^c O(g)_{aa'} O(g)_{bb'} &= \sigma_{a'b'}^{c_0}, \\ \sum_{abcd} O^T(g)_{c_0c} \sigma_{ab,d}^c O(g)_{aa'} O(g)_{bb'} \gamma(g)_{dd'} &= \sigma_{a'b',d'}^{c_0}. \end{aligned} \quad (33)$$

Let us consider the nonlinear optical response for the valley polarized order τ_z . The symmetry characters of the τ_z order are given by

$$\gamma(C_{3z}) = 1, \gamma(C_{2y}) = -1, \gamma(C_{2x}) = 1, \gamma(C_{2z}) = -1, \gamma(\mathcal{T}) = -1 \quad \text{for } \tau_z \text{ order parameter.} \quad (34)$$

The C_{3z} symmetry enforces

$$\begin{aligned} \sigma_{xx,0}^x &= -\sigma_{xy,0}^y = -\sigma_{yx,0}^y = -\sigma_{yy,0}^x, \\ \sigma_{xx,z}^x &= -\sigma_{xy,z}^y = -\sigma_{yx,z}^y = -\sigma_{yy,z}^x, \\ \sigma_{xx,0}^y &= \sigma_{xy,0}^x = -\sigma_{yx,0}^x = -\sigma_{yy,0}^y, \\ \sigma_{xx,z}^y &= \sigma_{xy,z}^x = -\sigma_{yx,z}^x = -\sigma_{yy,z}^y. \end{aligned} \quad (35)$$

The C_{2z} symmetry enforces $\sigma_{ab,0}^c$ to be vanishing, and C_{2x} enforces $\sigma_{xx,z}^y = 0$. Therefore, only $\sigma_{xx,z}^x = -\sigma_{xy,z}^y = -\sigma_{yx,z}^y = -\sigma_{yy,z}^x$ are the symmetry allowed photo conductivities in the nonlinear optical response in the valley polarized state. Clearly, this nonlinear optical response is induced by the valley polarization.

As for the σ_z sublattice polarized order parameter, the characters are

$$\gamma(C_{3z}) = 1, \gamma(C_{2y}) = -1, \gamma(C_{2x}) = -1, \gamma(C_{2z}) = -1, \gamma(\mathcal{T}) = 1 \quad \text{for } \sigma_z \text{ order parameter.} \quad (36)$$

Compared to τ_z order parameter, the C_{2x} symmetry allows the non-zero $\sigma_{xx,z}^y$. Thus, the nonlinear optical response with the σ_z order parameter becomes $\sigma_{xx,z}^x = -\sigma_{xy,z}^y = -\sigma_{yx,z}^y = -\sigma_{yy,z}^x$ and $\sigma_{xx,z}^y = \sigma_{xy,z}^x = -\sigma_{yx,z}^x = -\sigma_{yy,z}^y$.

If the order parameter is $\tau_z \sigma_x$, the characters become

$$\gamma(C_{3z}) = -1, \gamma(C_{2y}) = -1, \gamma(C_{2x}) = 1, \gamma(C_{2z}) = -1, \gamma(\mathcal{T}) = -1 \quad \text{for } \tau_z \sigma_x \text{ order parameter.} \quad (37)$$

Compared to τ_z order parameter, the $\tau_z\sigma_x$ order parameter breaks the C_{3z} symmetry and thus lost the symmetric restriction Eq.35. For the σ_y order parameter, the character of C_{2x} symmetry is $\gamma(C_{2x}) = -1$ which enforces $\sigma_{xx}^x = \sigma_{xy}^x = \sigma_{yx}^y = \sigma_{yy}^x = 0$.

The nonlinear photo conductivity can be derived based on time-dependent second-order perturbation theory, which can be written generally as following,

$$\begin{aligned} \sigma_{ab}^c(\nu'; \nu - \nu') &= \frac{e^3}{\hbar^2 \nu'(\nu - \nu')} \int \frac{d^3k}{(2\pi)^3} \sum_{nml} (f_{n\mathbf{k}} - f_{l\mathbf{k}}) \frac{v_{nm}^a v_{ml}^c v_{ln}^b}{(E_{l\mathbf{k}} - E_{n\mathbf{k}} - (\nu - \nu') - i\delta)(E_{l\mathbf{k}} - E_{m\mathbf{k}} - \nu - i\delta)} \\ &- \frac{e^3}{\hbar^2 \nu'(\nu - \nu')} \int \frac{d^3k}{(2\pi)^3} \sum_{nml} (f_{n\mathbf{k}} - f_{l\mathbf{k}}) \frac{v_{nm}^c v_{ml}^a v_{ln}^b}{(E_{l\mathbf{k}} - E_{n\mathbf{k}} - (\nu - \nu') - i\delta)(E_{m\mathbf{k}} - E_{n\mathbf{k}} - \nu - i\delta)}. \end{aligned} \quad (38)$$

where $v_{nl}^a = \langle u_{n\mathbf{k}} | \partial_{k_a} H_{\mathbf{k}} | u_{l\mathbf{k}} \rangle / \hbar$ is velocity martrix elements.

If $\nu=0$ and $\nu'=\hbar\omega$, this photon conductivity refers to the shift current possess. If $\nu=2\hbar\omega$ and $\nu'=\hbar\omega$, it represents the second harmonic generation. For the shift current, it can be re-written as

$$\begin{aligned} \sigma_{ab}^c(\omega) &= \frac{e^3}{\hbar^2 \omega^2} \int \frac{d^3k}{(2\pi)^3} \sum_{nml} (f_{n\mathbf{k}} - f_{l\mathbf{k}}) \frac{(v_{nl}^b v_{lm}^a v_{mn}^c)^*}{(E_{n\mathbf{k}} - E_{l\mathbf{k}} - \omega + i\delta)(E_{n\mathbf{k}} - E_{m\mathbf{k}} + i\delta)} \\ &+ \frac{e^3}{\hbar^2 \omega^2} \int \frac{d^3k}{(2\pi)^3} \sum_{nml} (f_{n\mathbf{k}} - f_{l\mathbf{k}}) \frac{v_{nl}^b v_{lm}^a v_{mn}^c}{(E_{n\mathbf{k}} - E_{l\mathbf{k}} + \omega - i\delta)(E_{n\mathbf{k}} - E_{m\mathbf{k}} - i\delta)}. \end{aligned} \quad (39)$$